applied sciences

MDPI

Article

Automatic Measurement of Contact Stress and Connection Force of Interference Components by Ultrasound

Xianrui He [1], Xingyuan Wang [1,*], Chonglin Xu [2] and Yue Wang [3]

[1] College of Mechanical and Electrical Engineering, Harbin Engineering University, Harbin 150001, China; hexianrui2002@hrbeu.edu.cn
[2] Institute of Materials, China Academy of Engineering Physics, Jiangyou 621908, China; xuclcaep@163.com
[3] Department of Biomedical Engineering, City University of Hong Kong, Kowloon, Hong Kong 999077, China; ywang2524-c@my.cityu.edu.hk
* Correspondence: xywang@hrbeu.edu.cn

Abstract: Tiny interference components play an important role in the aerospace and instrumentation fields. Contact stress and connection force are important factors in evaluating the reliability and service life of components. In this study, the ultrasonic method is used to measure the stress distribution and the connection force on the mating interface. Based on statistical microcontact theory, the virtual thin-layer model, and the asperity interaction model, the contact acoustic model is optimized. On this basis, the mapping relationship between contact stress and contact stiffness can be further obtained. This relationship was obtained by calibration experiments. Then, the stress distribution on the interface with two different structures, namely the uniform cylinder and the step cylinder, was measured and compared with the theoretical results of the thick-walled cylinder theory. The results show that the two have good consistency. Finally, based on the stress distribution, the connection force was calculated and compared with the experimental results. The results show that the ultrasonic measurement method can accurately measure the connection force, and the relative error is within 16%. Therefore, this study can provide a good method for the quality assessment of interference components.

Keywords: interference components; acoustic model; contact stress; connection force; ultrasonic wave

Citation: He, X.; Wang, X.; Xu, C.; Wang, Y. Automatic Measurement of Contact Stress and Connection Force of Interference Components by Ultrasound. *Appl. Sci.* **2023**, *13*, 12461. https://doi.org/10.3390/app132212461

Academic Editors: M. H. Ferri Aliabadi, Francesco Caputo and Alessandro De Luca

Received: 8 September 2023
Revised: 9 November 2023
Accepted: 10 November 2023
Published: 17 November 2023

1. Introduction

Tiny interference components are widely used in the precision connection of the aerospace and instrumentation fields. Assembly quality will greatly affect the performance and life of mechanical equipment [1–4]. The stress distribution and connection force are important parameters for evaluating assembly quality [1,5]. Therefore, studying the stress distribution and connection force on the mating surface of interference components is very important and promising to study. Ultrasonic methods to measure contact stresses have been widely used because ultrasonic waves can be flexibly applied to many practical engineering materials and components [6,7].

The ultrasonic measurement of contact stress can be achieved based on the mapping relationship of reflection coefficient-contact stiffness-contact stress. In the same contact state, ultrasonic waves with different frequencies have different wavelengths, which affects the amplitude of ultrasonic waves reflected from the contact interface, thereby changing the reflection coefficient. Therefore, the mapping relationship between the reflection coefficient and contact stress measured by ultrasonic transducers with different center frequencies is different. Fortunately, the mapping relationship between contact stiffness and contact stress is not affected by ultrasonic frequency. This is due to the fact that contact stiffness is a mechanical property of the contact interface and is not affected by the frequency of ultrasonic waves [8]. Based on the contact stiffness-contact stress mapping relationship, the contact stress measured by the ultrasonic transducer with different center frequencies

is consistent. Therefore, the calibration of the contact stiffness-contact stress mapping relationship can make the measurement of contact stress independent of frequency, which means the measurement results are unaffected even if transducers with different frequencies are used in the calibration and measurement stages. In practical engineering, the reflection coefficient—contact stress is calibrated first, and then the contact stiffness—contact stress is obtained by the contact acoustic model. As a result, the connection force can be calculated using Coulomb's friction law based on the measured stress distribution.

Several acoustic models have been developed over the past few decades [9–11]. Kendal and Tabor [10] proposed a spring model, which can be represented by a single spring, to describe the ultrasonic reflection from the stationary and sliding interfaces under the elastic contact assumption to determine the reflection coefficient and contact stiffness mapping relationship. Based on the spring model, Drinkwater et al. measured the contact stiffness of the Al–Al interface at different pressures [8]. Unfortunately, the measured stiffness is much higher than predicted by the theoretical contact model. In contrast, the GW model is in good agreement with the experiments performed using approximation measurements in the elastic deformation range [12]. This model is obtained by integrating the contact states of all asperities using statistical theory. This provides a more reasonable description of the actual contact state of the rough interface. However, this model does not give the relationship between contact stiffness and acoustic parameters.

Recently, methods based on virtual material assumptions [13,14] have been shown to be effective in describing contact properties in engineering applications, such as bolting [15]. However, these previous models were limited to dry, rough interfaces. In practical industrial applications, mechanical systems such as various gears, rolling bearings, and wheel–rail interfaces work in mixed lubricating contacts to reduce friction or wear; that is, lubricants fill concave valleys in rough interfaces. For the lubrication interface, the coupling effect of roughness and lubricant increases the difficulty of constructing the acoustic model. To solve this problem, Xiao and Sun [16] systematically studied the virtual interface layer model. A micro-contact acoustic model was constructed to analyze the contact stiffness of the rough lubrication interface, and the relationship between statistical parameters and contact state was obtained [17]. However, none of the above models consider the effect of asperity interaction on interface stiffness under lubrication conditions. Therefore, it is necessary to optimize the acoustic model to improve the measurement accuracy of stress distribution and connection force.

In this study, statistical micro-contact theory and the virtual thin-layer concept were used to optimize the contact acoustic model considering the asperity interaction. The mapping relationship between the reflection coefficient and contact stiffness is obtained by using the improved acoustic model. Then, the mapping relationship between contact stiffness and contact stress is determined by calibration experiments. Two interference components with different structures were measured using an automatic measurement setup, and the stress distribution on the mating surface was obtained and compared with the theoretical results. Finally, based on the stress distribution, the connection force is calculated and compared with the connection force measured by the press-out experiments.

2. Materials and Methods

2.1. Virtual Material-Based Acoustic Model

The thin layer of the rough surface is assumed as a virtual material with thickness h, elastic modulus E_0, shear modulus G_0, Poisson's ratio v_0, and density ρ_0, as shown in Figure 1. The thin layer is rigidly connected with the contacting body to ensure the continuous propagation of elastic waves. Therefore, the contacting bodies and the equivalent thin layer can be assumed as a multilayer system (see Figure 1).

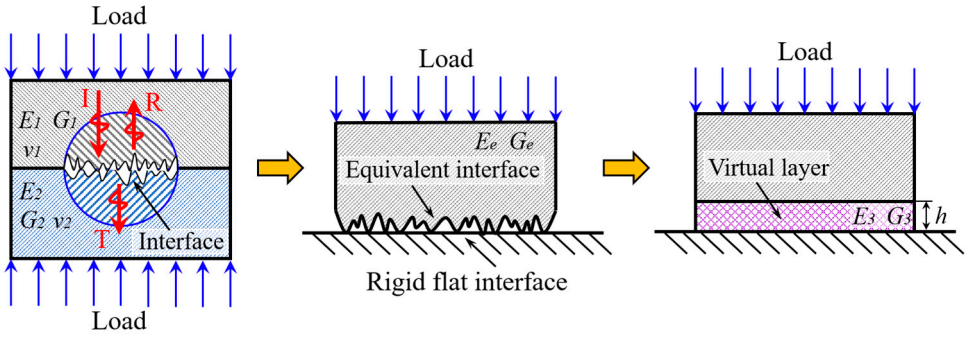

Figure 1. Rough interface represented by a thin layer of virtual material.

When the longitudinal wave incident is normal compared to the equivalent thin layer, the reflection coefficient at the contact interface can be expressed as [18]

$$R = \frac{\rho_0 c_0 \sin(\omega h/c_0) - (Z^2/\rho_0 c_0)\sin(\omega h/c_0)}{\rho_0 c_0 \sin(\omega h/c_0) + 2iZ\cos(\omega h/c_0) + (Z^2/\rho_0 c_0)\sin(\omega h/c_0)} \tag{1}$$

where ρ_0 is the density of the virtual material, c_0 is the longitudinal wave velocity of the virtual material, Z is the acoustic impedance of the contacting solid, ω is the angular frequency of ultrasound, h is the layer thickness, i.e., surface separation, and i is the imaginary unit. Since the thickness of the virtual thin layer is much smaller than the incident wavelength, Equation (1) can be simplified by asymptotic expansion and truncated to the first order [19]. Therefore, the reflection coefficient can be expressed as

$$R = \frac{\rho_0 h\omega - (Z^2\omega h/\rho_0 {c_0}^2)}{\rho_0 h\omega + (Z^2\omega h/\rho_0 {c_0}^2) + 2iZ} \tag{2}$$

where $\rho_0 h$ represents the influence of the mass on the virtual thin layer. However, the mass term is effective only when the thickness of the thin layer is large [20]. For general rough contacts, the interface contains low-density air gaps, and the virtual interface layer is very thin, which means that the interface mass term has almost no effect on the reflection coefficient. Therefore, the mass term, $\rho_0 h$, can be ignored, and Equation (2) can be written as

$$R = \frac{-Z\omega}{Z\omega + 2i\rho_0 {c_0}^2/h} \tag{3}$$

where $\rho_0 {c_0}^2/h$ represents the normal contact stiffness K_c per unit of nominal contact area. In this study, the virtual thin layer is assumed to be elastically deformed so that the contact stiffness K_c is real and can be written as Equation (4), which is the stiffness expression form of the quasi-static spring model [10].

$$K_c = \frac{Z\omega}{2}\sqrt{\frac{1}{|R|^2} - 1} \tag{4}$$

According to Equation (4), the thickness of the thin layer h can be deduced as

$$\frac{1}{h} = \frac{Z\omega}{2\rho_0 {c_0}^2}\sqrt{\frac{1}{|R|^2} - 1} \tag{5}$$

For the equivalent virtual thin layer, the normal contact stiffness K_n equals the ratio of elastic modulus E_0 to thickness h. Therefore, combining Equations (4) and (5), the interfacial normal contact stiffness can be expressed as [15]

$$K_n = \frac{E_0(3G_0 - E_0)}{G_0(4G_0 - E_0)} \frac{Z\omega}{2} \sqrt{\frac{1}{|R|^2} - 1} = \frac{E_0(3G_0 - E_0)}{G_0(4G_0 - E_0)} K_c \tag{6}$$

The rough contact interface is a mixed distribution of asperities and air gaps. Therefore, the equivalent material properties of the virtual thin layer need to be determined by integrating the mechanical properties of single asperities based on the statistical microcontact theory. As the asperity interaction will affect the asperity's deformation, the average interface separation and the interface stiffness, the solution of the mechanical properties of a single asperity needs to consider the effect of the asperity interaction. As shown in Figure 2, the total interference of a given asperity is δ, which includes two parts: deformation due to the contact load w and deformation due to asperity interactions u_g. Therefore, the construction of virtual material parameters should consider the effect of asperity interactions.

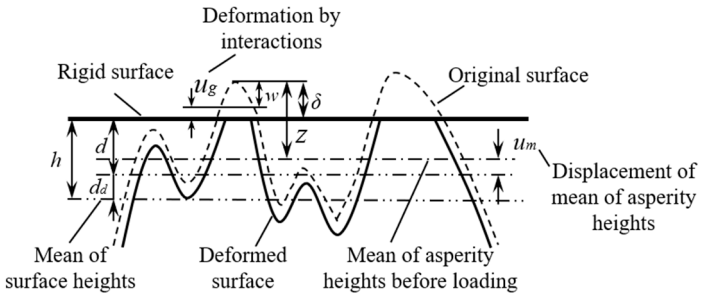

Figure 2. Rough surface deformation under asperity interactions.

2.1.1. Equivalent Shear Modulus

The ultrasonic attenuation generated from friction or adhesion between contacting asperities has a significant effect on the accuracy of acoustic model. The contacting asperities of the whole rough surface are misaligned to some degree, which gives rise to the frictional tangential motions and adhesion of contacting asperities and contribute to the ultrasound attenuation at the interface. The shear modulus g of the single asperity can be expressed as [15]

$$g = \frac{16G}{\pi} \left(1 - \frac{0.6S_y}{0.25} \frac{k_e}{E} \sqrt{\frac{\beta}{\sigma}}\right)^{\frac{1}{3}} \tag{7}$$

$$k_e = \frac{3\pi \int_0^\infty (z_n - h_n)\phi_n(z_n)dz_n}{4 \int_0^\infty (z_n - h_n)^{3/2}\phi_n(z_n)dz_n} \tag{8}$$

where S_y is the yield strength, β is the asperity radius of curvature, h_n is the ratio between h and σ (the standard deviation of the surface height distribution). ϕ_n (z_n) is the normalized probability density function of height distribution, which can be expressed as

$$\phi_n(z_n) = \frac{1}{\sqrt{2\pi}} \left(\frac{\sigma}{\sigma_s}\right) exp\left(-\frac{1}{2}\left(\frac{\sigma}{\sigma_s}\right)^2 z_n^2\right) \tag{9}$$

where $z_n = z/\sigma$ is the non-dimensional parameter, σ_s is the standard deviation of asperity heights distribution. The ratio of σ/σ_s for the isotropic rough surfaces with a Gaussian distribution of surface heights is

$$\sigma/\sigma_s = n\beta\sigma/\sqrt{(n\beta\sigma)^2 - \gamma} \tag{10}$$

where γ is a constant with $\gamma = 3.71693 \times 10^{-4}$, n is the asperity distribution density, and

$$\sigma = \sqrt{m_0} \quad n = \frac{m_4}{6\pi\sqrt{3}m_2} \quad \beta = 0.375\sqrt{\frac{\pi}{m_4}} \tag{11}$$

where m_0, m_2, m_4 are the spectral moments of the rough surface.

Equation (8) can be numerically calculated with h_n varying in the range of [0, 3] to cover all levels of real contacts. Since h_n is affected by asperity interactions, the premise of achieving k_e solution is to obtain h_n under different loads.

Accordingly, the shear modulus of the virtual material can be obtained by integrating the single asperity shear modulus with the number of contact asperities and is expressed as

$$G_0 = N\int_{h_n-d_n}^{\infty} g\phi_n(z_n)\mathrm{d}z_n \tag{12}$$

where $N = nA_n$ is the total number of asperities with the mean plane of the asperity heights taken as the reference plane, A_n is the nominal contact area, $d_n = d_d/\sigma$ is the dimensionless distance between the mean of asperity heights and that of surface heights. d_d is given by [17,21], and d_n can be expressed as

$$d_n = \frac{4m_2}{\sigma\sqrt{\pi m_4}} \tag{13}$$

2.1.2. Equivalent Elastic Modulus

Based on the Hertz elastic contact theory and the normal stress–strain relation of an asperity, the elasticity modulus of a single asperity can be expressed as

$$e = \frac{2E}{3\pi}\sqrt{\frac{\beta}{w}} \tag{14}$$

where w is the deflection of the asperity, which is affected by the asperity interactions (see Figure 2).

The elasticity modulus of virtual material can be expressed as

$$E_0 = N\int_{h_n-d_n}^{\infty} e\phi_n(z_n)\mathrm{d}z_n \tag{15}$$

Since the asperity interactions can increase the surface separation and reduce the asperity deflection, the calculation of E_0 should consider the influence of asperity interactions.

2.1.3. P_m-K_n-R Relationship Considering Asperity Interactions

Considering the influence of asperity interactions, the asperity deformation due to the contact load can be expressed as

$$w = z + d_d - h + \left(u_m - u_g\right) \tag{16}$$

where u_m is the displacement of the mean of asperity heights. According to the asperity interactions model proposed by [22], the deflection of the asperity can be expressed as

$$w = z + d_d - h + 1.3\sqrt{\beta^{1/2}w^{3/2}\frac{p_m}{E}} \tag{17}$$

where p_m is the global mean contact stress. All the length parameters and variables in Equation (17) are normalized by dividing σ. The resulting dimensionless equation is given by

$$w_n = z_n + d_n - h_n + 1.3\sqrt{\beta^{1/2}w^{3/2}\frac{p_m}{E}} \tag{18}$$

Combining Equations (5), (14)–(17), the elasticity modulus can be expressed as

$$E_0 = \frac{2NE}{3\pi}\sqrt{\frac{\beta}{\sigma}}\int_{h_n-d_n}^{\infty} {w_n}^{-1/2}\phi_n(z_n)\mathrm{d}z_n \tag{19}$$

With the ZMC model [23], the dimensionless contact load W_{tn} can be expressed as

$$W_{tn} = \frac{p_m}{E} = \frac{4n\sigma\beta}{3\pi}\sqrt{\frac{\sigma}{\beta}}\int_{h_n-d_n}^{\infty} {w_n}^{3/2}\varnothing_n(z_n)\mathrm{d}z_n \tag{20}$$

Since the contact load W_{tn} and surface separation h_n are coupled together, the Newton–Raphson iterative formula and five-point Legendre–Gaussian quadrature are used to solve the above governing equations. As a result, the relationship of P_m-K_n-R can be obtained.

The following describes the computational procedure in this work.

1. Input parameters of the problem (m_0, m_2, m_4, R, E, G, S_y, A_n).
2. For a given load W_{tn}, the value of w_n as a function of h_n and z_n can be solved from Equation (18) using the Newton–Raphson iterative formula.
3. By adjusting the value of h_n, the calculated load of Equation (20) using the five-point Legendre–Gaussian quadrature can be made equal to the given load, and the relation between W_{tn} and h_n can also be determined.
4. By selecting a different load, the corresponding mean separation h_n can be obtained following steps 2 and 3. Therefore, the relations between P_m and h_n and between P_m and R can be obtained.
5. Substituting h_n into Equation (19), E_0 can be calculated using the five-point Legendre–Gaussian quadrature. G_0 can be obtained by integrating Equation (12).
6. Finally, R, E_0 and G_0 are substituted into Equations (4) and (6) to calculate the contact stiffness K_n under the given contact condition, and the relation of P_m-K_n-R can be determined.

2.2. Experiments

In this study, the stress distribution and connection force of two types of interference components were measured (see Figure 3). The shaft and hub are made of AISI 1045 steel ($E_1 = E_2 = 2.09 \times 10^{11}$ Pa, $G_1 = G_2 = 7.69 \times 10^{10}$ Pa, $v_1 = v_2 = 0.29$). The statistical topography parameters of the contact surface and the equivalent rough surface were calculated, and the results are shown in Table 1. The reflection coefficient is affected by the acoustic frequency, but the interface stiffness is not. Therefore, to achieve the contact stress measurement, it is necessary to calibrate the relationship P_m-K_n, which can be obtained by the improved acoustic model. To evaluate the connection quality, the connection force was calculated and verified by the press-out experiments. Therefore, the experiment of this study consists of three parts: calibration experiment, stress measurement experiment, and connection force measurement experiment.

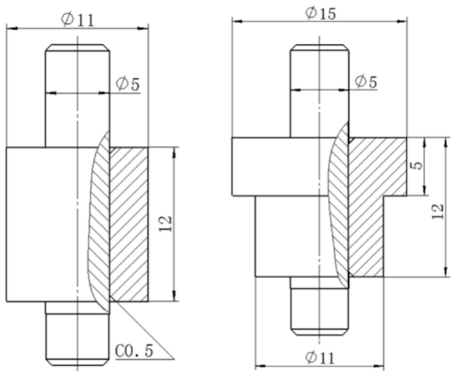

Figure 3. Structural dimensions of interference components: (**a**) uniform cylinder, (**b**) step cylinder.

Table 1. Statistical parameters of rough surfaces.

Samples	m_0 (μm^2)	m_2	m_4 (μm^{-2})	n (μm^{-2})	β (μm)	σ (μm)
Shaft	2.96×10^{-2}	3.36×10^{-4}	1.89×10^{-5}	1.96×10^{-3}	159.67	1.69×10^{-1}
Hub	1.72×10^{-1}	1.27×10^{-3}	6.57×10^{-5}	1.59×10^{-3}	82.28	4.14×10^{-1}
Equivalent	2.02×10^{-2}	1.60×10^{-3}	8.45×10^{-5}	1.60×10^{-3}	72.30	4.49×10^{-1}

2.2.1. Experimental Setup

The calibration setup is mainly composed of an ultrasonic transducer, an ultrasonic pulse generator receiver, a digital oscilloscope, a measurement module, a transducer adjustment module, a force application device, and an industrial computer (as shown in Figure 4). The press-out experiment also can be carried out using this setup to measure the connection force. The reflection coefficient under different loads can be obtained by applying different loads to the force loading tube. It should be noted that the calibrated interface should be consistent with the topography characteristics of the tested interface. The center frequency of the point-focused immersion transducer is 10 MHz, and the wafer radius r_p is 3 mm. The roughness Ra of the upper and lower test plates are 0.09 μm and 0.3 μm, respectively. The contact area, A_n, of the two calibration plates is 38.48 mm^2.

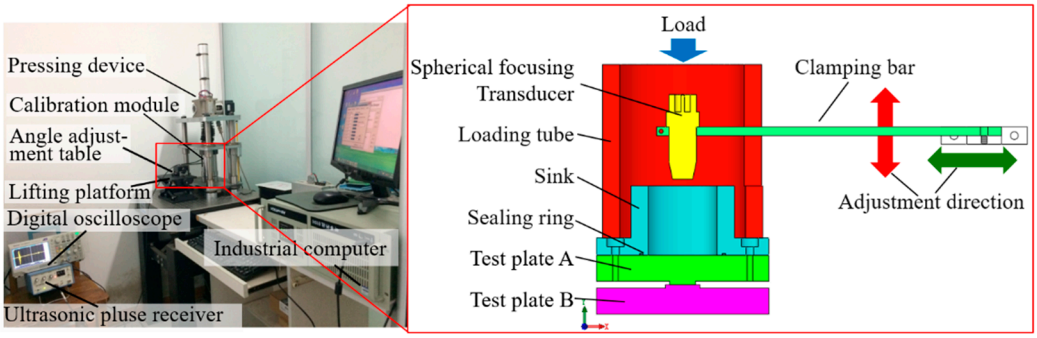

Figure 4. Schematic diagram of the calibration setup.

The stress-distribution measurement setup is shown in Figure 5. The setup is mainly composed of a point-focused immersion transducer, an ultrasonic pulse receiver, a digital oscilloscope, a motion control module, a clamping module, an adjustment module, and an industrial computer. The function of the motion control module is to perform motion control on the interference components, thus enabling a full-coverage scan of the entire mating surface (see Figure 6). The clamping module is to ensure the reliable clamping and positioning of components. The adjustment module is to adjust the inclination of the transducer so that the sound beam can irradiate the mating surface vertically. The digital oscilloscope can display the received ultrasonic signal in real time and transmit the data to the computer for signal processing, analysis, and storage.

The motion control module consists of XYZ linear stages (GCD-202150M, Daheng Optics, Beijing, China: repeatable positioning accuracy < 5 μm, resolution 1 μm) and a precision turntable (RAK100, Zolix, Beijing, China: repeatability < 0.005°, radial runout < 20 μm, resolution 0.00125° under eight subdivisions), which can control the translation of interference components in the X, Y, and Z directions and the rotation around the Z axis. The position of the transducer relative to the interference components can be adjusted by the XYZ linear stages. The clamping module consists of two V-blocks, which are installed on the precision turntable. The adjustment module consists of two goniometers on which the transducer is mounted via a clamping rod.

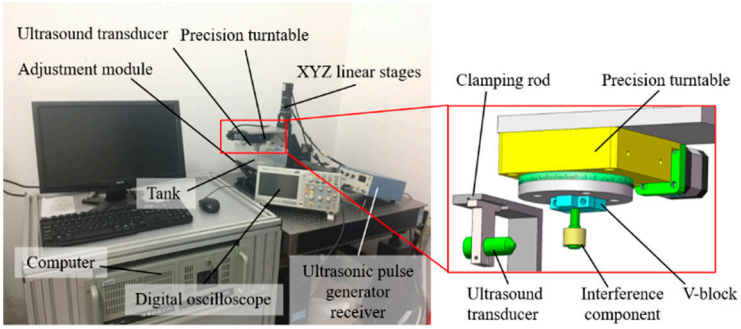

Figure 5. Interference component stress-distribution measuring device.

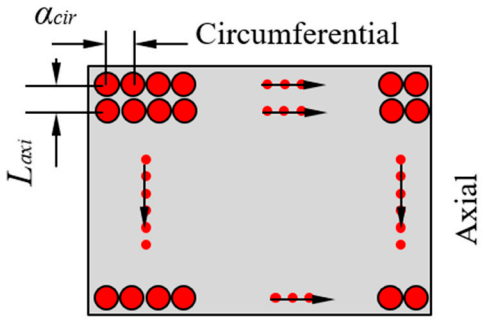

Figure 6. Scanning scheme of stress distribution on mating surface.

To ensure the acoustic beam vertically focused on the mating interface, the alignment of the transducer and the component is necessary, as shown in Figure 7. α are β are the incidence and refraction angles of the ultrasonic wave. γ is the angle between the normal of the incident point and the acoustic beam axis. The depth of the coupling agent is calculated according to Equation (21), and the position of the interference component in the Y direction is adjusted according to the arriving time of the echo reflected from the coupling agent–component interface on the digital oscilloscope. Then, the interference component is fine-tuned in the Y direction until the signal reflected at the interface is maximized.

$$\begin{cases} a = F_C - h_h - \frac{mq}{k\xi \sin\varepsilon - \zeta} \\ m = R_0 + a - F_C \\ \xi = \sin\varepsilon - \frac{F_C - a}{R}\sin\varepsilon \\ \zeta = \left(\sqrt{1-\xi^2}\sin\varepsilon - \xi\cos\varepsilon\right)\left(k\xi\sqrt{1-\xi^2} - \xi\sqrt{1-(k\xi)^2}\right) \end{cases} \tag{21}$$

where a is the depth of the couplant; F_C is the focal length in the coupling agent; h_h is the thickness of the cylinder; m is the distance from the original focus M to the cylinder axis; $k = C_s/C_c$ is the refractive index (C_c is the wave velocity in the coupling agent; C_s is the wave speed in a solid); R_0 is the radius of the cylinder; ε is half the beam angle.

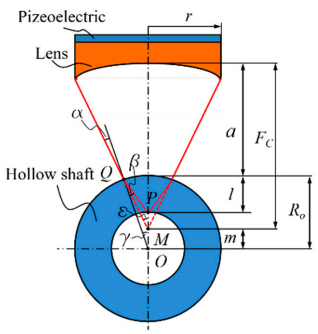

Figure 7. The relative position of the transducer to the component.

2.2.2. Measurement of Stress Distribution

The measurement of stress distribution on the mating surface mainly includes the following three steps: the calibration of P_m-K_n, the measurement of the reflection coefficient, and the calculation of stress distribution.

1. Calibration of P_m-K_n: In order to achieve a reliable measurement of the stress distribution on the mating interface, the equipment in Figure 4 is used to calibrate the P_m-K_n relationship, and kerosene is used as the coupling agent in the calibration experiment. The calibration results are shown in Figure 8. The R-P_m curve was obtained by calibration experiments. Then, K_c-P_m and P_m-K_n curves were calculated according to Equations (4) and (6). Obviously, the reflection coefficient is negatively correlated with the contact stress. This is due to the fact that the increase in contact stress increases the actual contact area of the rough interface, resulting in more ultrasonic transmission. As a result, the ultrasonic amplitude reflected from the rough interface is weakened, thus reducing the reflection coefficient. On the other hand, with the increase in the actual contact area, the bearing capacity of the rough interface gradually increases; that is, the ability to resist deformation increases. Therefore, the contact stiffness of the rough interface is positively correlated with the contact stress. In addition, it can also be found that $K_c > K_n$. This is due to the interaction between asperities. The asperities in the interface will bear the load together; the interaction behavior will reduce the interface deformation and the actual contact area. As a result, the reflection coefficient of the rough interface is weakened. According to the above analysis, the contact stiffness will decrease. Therefore, the contact stiffness obtained by Equation (4) is greater than that obtained by Equation (6), i.e., $K_c > K_n$. The relative error of the two contact stiffnesses is about 10%. Therefore, the accuracy of the connection force can be improved by about 10% by using the proposed acoustic model.

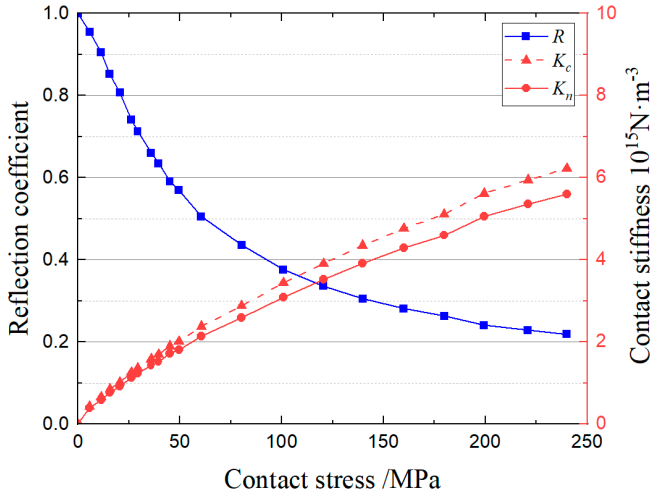

Figure 8. Calibration results of contact stress interface stiffness.

2. Measurement of reflection coefficient: The reflection coefficient is the ratio of the amplitude of the reference signal to the reflected signal at the interface. The reference signal is the signal reflected from the inner surface of the hub when it is not assembled. The reflected signal is the signal reflected from the mating interface. According to the distribution of the reflected signal at the interface, the reflection coefficient distribution can be obtained.
3. Stress distribution on the mating interface: The reflection coefficient distribution and the relationship between contact stress and interface stiffness have been obtained through the previous experiments. The calibration results are shown in Figure 8. According to the reflection coefficient distribution and the P_m-K_n mapping relationship, the stress distribution of the mating surface can be obtained.

2.2.3. Analysis of Connection Force

The connection force of interference components is calculated according to Coulomb's law of friction. Since the stress distribution on the mating interface has been measured, it is necessary to measure the static friction coefficient.

1. Measurement of static friction coefficient: In order to obtain the connection force, the setup in Figure 4 was used to carry out the press-out experiments to measure the maximum press-out force, i.e., the connection force. According to Coulomb's law of friction, the static friction coefficient can be expressed as

$$f_s = F_{out} / \left(\sum_{i=1}^{N} P_i \frac{S_c}{N} \right) \tag{22}$$

where N is the number of scanning points on the contact interface; S_c is the contact area; P_i is the contact stress at the ith measurement point. The average static friction coefficient at the oil-lubricated interface is 0.1483.

2. Calculation of connection force: By substituting the stress distribution and static friction coefficient into Equation (23), the connection force can be obtained.

$$F_{con} = f_{s\_mean} \left(\sum_{i=1}^{N} P_i \frac{S_c}{N} \right) \tag{23}$$

3. Results and Discussion

To verify the improved acoustic model, the stress distribution measured by ultrasound is compared with the thick-walled cylinder theory. At the same time, the calculation results of the connection force were verified by press-out experiments.

3.1. Thick-Walled Cylinder Theory

As shown in Figure 9, this study involves a two-layer combined cylinder. The interference is $2I_r$. The normal contact stress is P. u_1 and u_2 are the deformation of the mating surface of the hollow shaft and hub, respectively. The normal contact stress of the non-mating surface is zero. Therefore, the contact stress of the interface can be expressed as

$$P = \frac{I_r}{\frac{r_2}{E_1}\left(\frac{r_1^2+r_2^2}{r_2^2-r_1^2} - \nu_1\right) + \frac{r_2}{E_2}\left(\frac{r_3^2+r_2^2}{r_3^2-r_2^2} + \nu_2\right)} \tag{24}$$

where E_1 and E_2 are the elastic modulus of the hollow shaft and hub, respectively. ν_1 and ν_2 are Poisson ratios of hollow shaft and hub, respectively. In this study, $E_1 = E_2$ and $\nu_1 = \nu_2$.

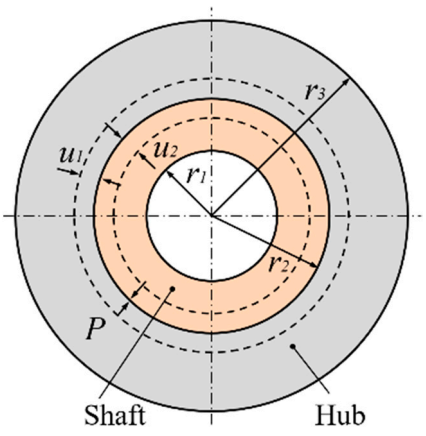

Figure 9. Two-layer combined cylinder.

3.2. Contact Stress Distribution

The reflection coefficient distribution of the component is shown in Figure 10. A strip bulge along the axial direction is observed, which indicates that there is wear on the mating interface during the pressing process. As shown in Figure 10b, the reflection coefficient of the thin-walled section is larger than that of the thick-walled section, which indicates that the contact stress of the thin-walled section is relatively small, which is consistent with the actual situation.

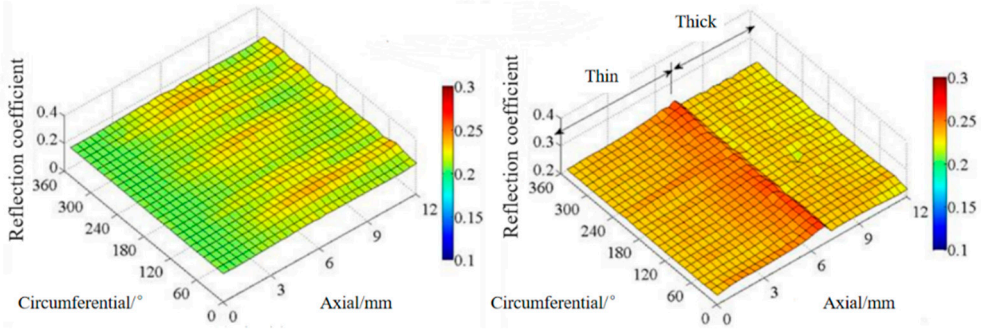

Figure 10. Distribution of reflection coefficients: (**a**) uniform cylinder, (**b**) step cylinder.

The stress distribution is shown in Figure 11. The contact stress of the uniform cylinder is basically the same as that of the thin-walled section of the step cylinder. In addition, the stress of the thick-walled section is greater than that of the thin-walled section, because the increase in the wall thickness leads to an increase in structural stiffness, which leads to a larger radial strain at the mating surface. In order to analyze the measurement accuracy, the average stress distribution along the axis was calculated and compared with the analytical result of the thick-walled cylinder theory, as shown in Figure 12. As can be seen from the figure, the relative errors δ of the measurement results of the two structures are within 20%.

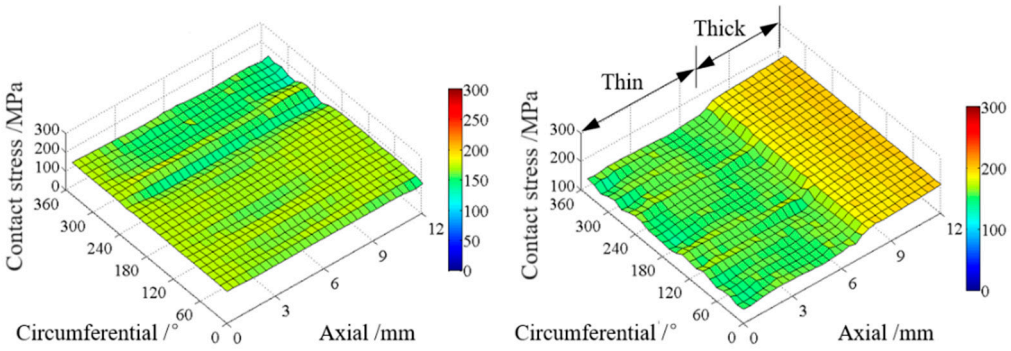

Figure 11. Distribution of contact stress: (**a**) uniform cylinder, (**b**) step cylinder.

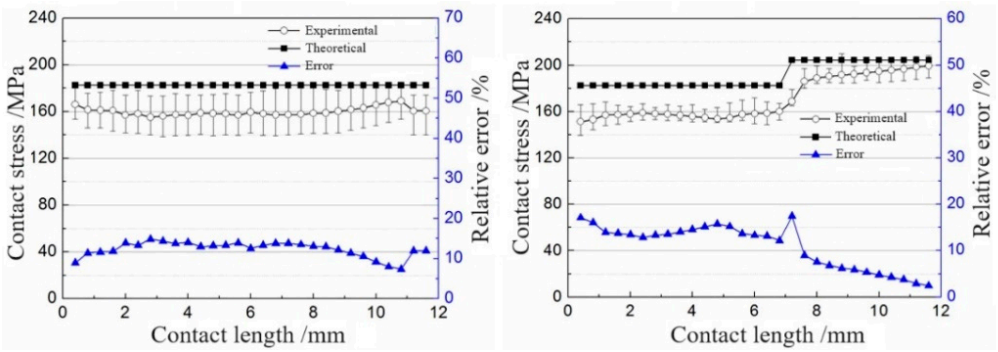

Figure 12. Measurement accuracy with different geometric shapes.

3.3. Connection Force

The connection force obtained by the press-out experiment and ultrasonic measurement is shown in Figure 13. The results show that the ultrasonic measurement error is within 16%. However, the measurement error of the No. 10 uniform cylinder reached 29.29%. The reason for the relatively large error is the serious interface wear during the press-fit process (see Figure 14). Coil chips on this part indicate severe wear at the interface. The stress-distribution map shows several wide and deep furrows on the mating interface, which aggravates the non-uniformity of stress distribution. Therefore, interface wear will significantly affect the contact state and change the static friction coefficient of the interface. In order to verify the above analysis, the static friction coefficient of this component was calculated as 0.1147, which is less than the average static friction coefficient of 0.1483. Therefore, the reliability of the calculation results should be analyzed according to the wear condition of the interface.

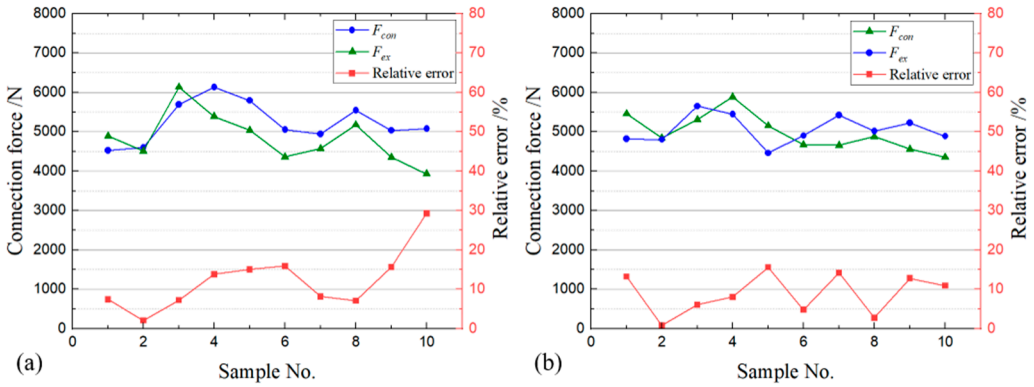

Figure 13. Calculation results of the connection force: (**a**) uniform cylinder, (**b**) step cylinder.

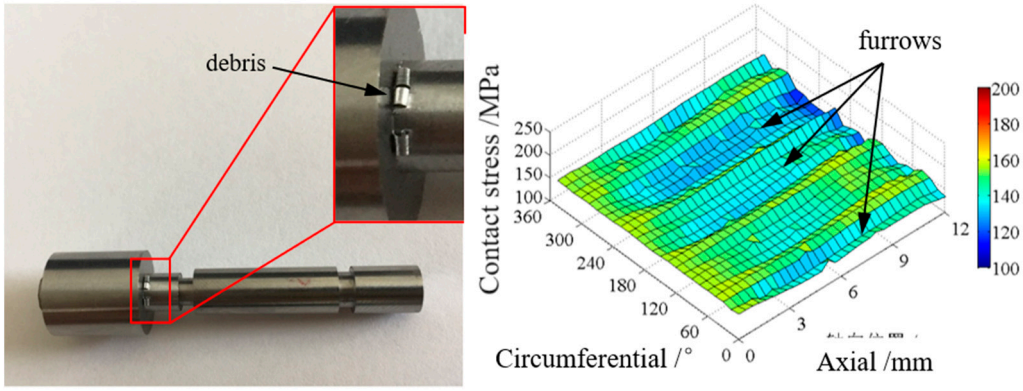

Figure 14. Wear component and stress distribution.

4. Conclusions

In order to achieve the measurement of contact stress and connection force, the acoustic model was improved. This acoustic model reveals the mapping relationship of P_m-K_n-R. A calibration setup was built to obtain the relationship between contact stiffness and contact stress. Then, the stress distribution on the mating surface of the uniform cylinder, and the stepped cylinder was measured and compared with the theoretical results. The relative error is within 20%. According to the stress distribution, the connection force was calculated and compared with the connection force measured by the press-out experiments. Except for the components with severe interface wear, the relative error of the connection force is less than 16%. Therefore, the improved acoustic model proposed in this paper provides an effective method for measuring the stress distribution and connection force of interference components. This is of great significance for improving the reliability of connection quality assessment.

Author Contributions: Conceptualization X.W. and C.X.; methodology, X.W. and X.H.; formal analysis, X.H. and X.W.; investigation, X.H.; resources, X.H. and X.W.; data curation, X.H., X.W. and Y.W.; writing—original draft preparation, X.H.; writing—review and editing, X.W. and C.X.; visualization, Y.W.; supervision, X.W.; project administration, X.W.; funding acquisition, X.W. All authors have read and agreed to the published version of the manuscript.

Funding: This research was supported by the National Natural Science Foundation of China (No. 52105544).

Institutional Review Board Statement: Not applicable.

Informed Consent Statement: Not applicable.

Data Availability Statement: The data presented in this study are available on request from the corresponding author. The data are not publicly available due to privacy restrictions request.

Conflicts of Interest: The authors declare no conflict of interest.

References

1. You, B.; Lou, Z.; Luo, Y.; Xu, Y.; Wang, X. Prediction of Pressing Quality for Press-Fit Assembly Based on Press-Fit Curve and Maximum Press-Mounting Force. *Int. J. Aerosp. Eng.* **2015**, *2015*, 823019. [CrossRef]
2. Marshall, M.B.; Lewis, R.; Dwyer-Joyce, R.S.; Demilly, F.; Flament, Y. Ultrasonic measurement of railway wheel hub–axle press-fit contact pressures. *Proc. Inst. Mech. Eng. Part F J. Rail Rapid Transit* **2011**, *225*, 287–298. [CrossRef]
3. Wang, X.Y.; Lou, Z.F.; Wang, X.D.; Xu, C.L. A new analytical method for press-fit curve prediction of interference fitting parts. *J. Mater. Process. Technol.* **2017**, *250*, 16–24. [CrossRef]
4. Wang, X.; Wang, Y.; Zhang, L.; Lou, Z. Press-fit analysis of multilayer interference fit. *Proc. Inst. Mech. Eng. C J. Mech. Eng. Sci.* **2022**, *237*, 903–918. [CrossRef]
5. Wang, X.; Liu, J.; Lu, S.; Wang, Y.; Wang, X.; Lou, Z.; Zhang, L. Connection force measurement of precision small interference components using ultrasound. *Proc. Inst. Mech. Eng. C J. Mech. Eng. Sci.* **2023**, 09544062231179085. [CrossRef]
6. Dwyer-Joyce, R.S. The Application of Ultrasonic NDT Techniques in Tribology. *Proc. Inst. Mech. Eng. Part J J. Eng. Tribol.* **2005**, *219*, 347–366. [CrossRef]
7. Aymerich, F.; Pau, M. Assessment of Nominal Contact Area Parameters by Means of Ultrasonic Waves. *J. Tribol.* **2004**, *126*, 639–645. [CrossRef]
8. Drinkwater, B.W.; Dwyer-Joyce, R.S.; Cawley, P. A study of the interaction between ultrasound and a partially contacting solid-solid interface. *Proc. Math. Phys. Eng. Sci.* **1997**, *452*, 2613–2628. [CrossRef]
9. Krolikowski, J.; Szczepek, J. Prediction of contact parameters using ultrasonic method. *Wear* **1991**, *148*, 181–195. [CrossRef]
10. Kendall, K.; Tabor, D. An utrasonic study of the area of contact between stationary and sliding surfaces. *Proc. R. Soc. Lond. Ser. A* **1971**, *323*, 321–340.
11. Balk, J.M.; Thompson, R.B. Ultrasonic scattering from imperfect interfaces a quasi-static model. *J. Nondestruct. Eval.* **1984**, *4*, 177–196.
12. Greenwood, J.A.; Williamson, J.B.P. Contact of nominally flat surfaces. *Proc. R. Soc. Lond. Ser. A Math. Phys. Sci.* **1966**, *295*, 300–319. [CrossRef]
13. Tian, H.; Li, B.; Liu, H.; Mao, K.; Peng, F.; Huang, X. A new method of virtual material hypothesis-based dynamic modeling on fixed joint interface in machine tools. *Int. J. Mach. Tools Manuf.* **2011**, *51*, 239–249. [CrossRef]
14. Ye, H.; Huang, Y.; Li, P.; Li, Y.; Bai, L. Virtual material parameter acquisition based on the basic characteristics of the bolt joint interfaces. *Tribol. Int.* **2016**, *95*, 109–117. [CrossRef]
15. Xiao, H.; Sun, Y. An improved virtual material based acoustic model for contact stiffness measurement of rough interface using ultrasound technique. *Int. J. Solids Struct.* **2018**, *155*, 240–247. [CrossRef]
16. Sun, Y.; Chuang, H.-C.; Xiao, H.; Xu, J. Prediction of the normal contact stiffness between elastic rough surfaces in lubricated contact via an equivalent thin layer. *J. Vib. Control* **2020**, *26*, 2060–2069. [CrossRef]
17. McCool, J.I. Relating profile instrument measurements to the functional performance of rough surfaces. *J. Tribol.* **1987**, *109*, 264–270. [CrossRef]
18. Lowe, M.J.S. Matrix techniques for modeling ultrasonic waves in multilayered media. *IEEE Trans. Ultrason. Ferroelectr. Freq. Control* **1995**, *42*, 525–542. [CrossRef]
19. Du, F.; Hong, J.; Xu, Y. An acoustic model for stiffness measurement of tribological interface using ultrasound. *Tribol. Int.* **2014**, *73*, 70–77. [CrossRef]
20. Margetan, F.J.; Thompson, R.B.; Rose, J.H.; Gray, T.A. The interaction of ultrasound with imperfect interfaces-experimental studies of model structures. *J. Nondestruct. Eval.* **1992**, *11*, 109–126. [CrossRef]
21. McCool, J.I. Predicting microfracture in ceramics via a microcontact model. *ASME J. Tribol.* **1986**, *108*, 380–386. [CrossRef]

22. Zhao, Y.; Chang, L. A Model of Asperity Interactions in Elastic-Plastic Contact of Rough Surfaces. *J. Tribol.* **2001**, *123*, 857–864. [CrossRef]
23. Zhao, Y.; Maietta, D.M.; Chang, L. An Asperity Microcontact Model Incorporating the Transition From Elastic Deformation to Fully Plastic Flow. *J. Tribol.* **2000**, *122*, 86–93. [CrossRef]